

Inclusive V^0 Production Cross Sections from 920 GeV Fixed Target Proton-Nucleus Collisions

The HERA-B Collaboration

I. Abt²⁸, A. Abyzov²⁶, M. Adams¹¹, H. Albrecht¹³, V. Amaral⁸, A. Amorim⁸, S. J. Aplin¹³, A. Arefiev²⁵, I. Ariño², M. Atiya³⁶, V. Aushev¹⁸, Y. Bagaturia^{13,43}, R. Baghshetsyan^{13,44}, V. Balagura²⁵, M. Bargiotti⁶, S. Barsuk²⁵, O. Barsukova²⁶, V. Bassetti¹², J. Bastos⁸, C. Bauer¹⁵, Th. S. Bauer^{32,33}, M. Beck³⁰, A. Belkov²⁶, Ar. Belkov²⁶, I. Belotelov²⁶, I. Belyaev²⁵, K. Berkhan³⁴, A. Bertin⁶, B. Bobchenko²⁵, M. Böcker¹¹, A. Bogatyrev²⁵, G. Bohm³⁴, C. Borgmeier⁵, M. Bräuer¹⁵, D. Broemmelsiek¹², M. Bruinsma^{32,33}, M. Bruschi⁶, P. Buchholz¹¹, M. Buchler¹⁰, T. Buran²⁹, M. Capeáns¹³, M. Capponi⁶, J. Carvalho⁸, J. Chamanina²⁷, B. X. Chen⁴, R. Chistov²⁵, M. Chmeissani², A. Christensen²⁹, P. Conde², C. Cruse¹¹, M. Dam⁹, K. M. Danielsen²⁹, M. Danilov²⁵, S. De Castro⁶, H. Deckers⁵, K. Dehmelt¹³, H. Deppe¹⁶, B. Dolgoshein²⁷, X. Dong³, H. B. Dreis¹⁶, M. Dressel²⁸, D. Dujmic¹, R. Eckmann¹, V. Egorytchev¹³, K. Ehret^{15,11}, V. Eiges²⁵, F. Eisele¹⁶, D. Emelianov¹³, S. Erhan²², S. Essenov²⁵, L. Fabbri⁶, P. Faccioli⁶, W. Fallot-Burghardt¹⁵, M. Feuerstack-Raible¹⁶, J. Flammer¹³, H. Fleckenstein¹³, B. Fominykh²⁵, S. Fourletov²⁷, T. Fuljahn¹³, M. Funcke¹¹, D. Galli⁶, A. Garcia², Ll. Garrido², D. Gascon², A. Gellrich^{34,5,13}, K. E. K. Gerndt¹³, B. Giacobbe⁶, J. Gläβ²⁴, T. Glebe¹⁵, D. Goloubkov^{13,39}, A. Golutvin²⁵, I. Golutvin²⁶, I. Gorbounov³¹, A. Gorišek¹⁹, O. Gouchtchine²⁵, D. C. Goulart⁷, S. Gradl¹⁶, W. Gradl¹⁶, Yu. Guilitzky^{25,13,41}, T. Hamacher^{13,1}, J. D. Hansen⁹, R. Harr¹⁰, C. Hast¹³, S. Hausmann¹⁶, J. M. Hernández^{13,34}, M. Hildebrandt¹⁶, A. Hölscher¹⁶, K. Höpfner¹³, W. Hofmann¹⁵, M. Hohlmann¹³, T. Hott¹⁶, W. Hulsbergen³³, U. Husemann¹¹, O. Igonkina²⁵, M. Ispiryan¹⁷, S. İşsever¹¹, H. Itterbeck¹³, J. Ivarsson^{23,34}, T. Jagla¹⁵, Y. Jia³, C. Jiang³, A. Kaoukher^{27,30}, H. Kapitza¹¹, S. Karabekyan^{13,44}, P. Karchin¹⁰, N. Karpenko²⁶, Z. Ke³, S. Keller³¹, F. Khasanov²⁵, H. Kim¹, Yu. Kiryushin²⁶, I. Kisel²⁸, F. Klefenz¹⁵, K. T. Knöpfle¹⁵, V. Kochetkov²⁵, H. Kolanoski⁵, S. Korpar^{21,19}, C. Krauss¹⁶, P. Kreuzer^{22,13}, P. Križan^{20,19}, D. Krücker⁵, T. Kvaratskheliia²⁵, A. Lange³¹, A. Lanyov²⁶, K. Lau¹⁷, G. Leffers¹⁵, I. Legrand³⁴, B. Lewendel¹³, Y. Q. Liu⁴, T. Lohse⁵, R. Loke⁵, B. Lomonosov^{13,38}, J. Lüdemann¹³, R. Männer²⁴, R. Mankel⁵, U. Marconi⁶, S. Masciocchi²⁸, I. Massa⁶, I. Matchikhilian²⁵, G. Medin⁵, M. Medinnis^{13,22}, M. Mevius³², A. Michetti¹³, Yu. Mikhailov^{25,13,41}, R. Miquel², R. Mizuk²⁵, A. Mohapatra⁷, A. Moshkin²⁶, B. Moshous²⁸, R. Muresan⁹, S. Nam¹⁰, M. Negodaev^{13,38}, I. Négre¹³, M. Nörenberg¹³, S. Nowak³⁴, M. T. Núñez Pardo de Vera¹³, T. Oest^{14,13}, A. Oliveira⁸, M. Ouchrif^{32,33}, F. Ould-Saada²⁹, C. Padilla¹³, P. Pakhlov²⁵, Yu. Pavlenko¹⁸, D. Peralta², R. Pernack³⁰, T. Perschke²⁸, R. Pestotnik¹⁹, B. AA. Petersen⁹, M. Piccinini⁶, M. A. Pleier¹⁵, M. Poli³⁷, V. Popov²⁵, A. Pose³⁴, D. Pose^{26,16}, I. Potashnikova¹⁵, V. Pugatch^{15,18}, Y. Pylypchenko²⁹, J. Pyrlik¹⁷, S. Ramachandran¹⁷, F. Ratnikov^{13,25}, K. Reeves^{1,15}, D. Reβing¹³, K. Riechmann²⁸, J. Rieling¹⁵, M. Rietz²⁸, I. Riu¹³, P. Robmann³⁵, J. Rosen¹², Ch. Rothe¹³, W. Ruckstuhl^{33,†}, V. Rusinov²⁵, V. Rybnikov¹³, D. Ryzhikov^{13,40},

F. Saadi-Lüdemann¹³, D. Samtleben¹⁴, F. Sánchez^{13,15}, M. Sang²⁸, V. Saveliev²⁷, A. Sbrizzi³³, S. Schaller²⁸, P. Schlein²², M. Schmelling¹⁵, B. Schmidt^{13,16}, S. Schmidt⁹, W. Schmidt-Parzefall¹⁴, A. Schreiner³⁴, H. Schröder^{13,30}, H.D. Schultz¹³, U. Schwanke³⁴, A. J. Schwartz⁷, A. S. Schwarz¹³, B. Schwenninger¹¹, B. Schwingenheuer¹⁵, R. Schwitters¹, F. Sciacca¹⁵, S. Semenov²⁵, N. Semprini-Cesari⁶, E. Sexauer¹⁵, L. Seybold¹⁵, J. Shiu¹⁰, S. Shuvalov^{25,5}, I. Siccama¹³, D. Škrk¹⁹, L. Sözüer¹³, A. Soldatov^{25,13,41}, S. Solunin²⁶, A. Somov^{5,13}, S. Somov^{13,39}, V. Souvorov³⁴, M. Spahn¹⁵, J. Spengler¹⁵, R. Spighi⁶, A. Spiridonov^{34,25}, S. Spratte¹¹, A. Stanovnik^{20,19}, M. Starić¹⁹, R. StDenis^{28,15}, C. Stegmann^{34,5}, S. Steinbeck¹⁴, O. Steinkamp³³, D. Stieler³¹, U. Straumann¹⁶, F. Sun³⁴, H. Sun³, M. Symalla¹¹, S. Takach¹⁰, N. Tesch¹³, H. Thurn¹³, I. Tikhomirov²⁵, M. Titov²⁵, U. Trunk¹⁵, P. Truöl³⁵, I. Tsakov^{13,42}, U. Uwer^{5,16}, V. Vagnoni⁶, C. van Eldik¹¹, R. van Staa¹⁴, Yu. Vassiliev^{18,11}, M. Villa⁶, A. Vitale⁶, I. Vukotic⁵, G. Wagner¹³, W. Wagner²⁸, H. Wahlberg³², A. H. Walenta³¹, M. Walter³⁴, T. Walter³⁵, J. J. Wang⁴, Y. M. Wang⁴, R. Wanke¹⁵, D. Wegener¹¹, U. Werthenbach³¹, P. J. Weyers⁵, H. Wolters⁸, R. Wurth¹³, A. Wurz²⁴, S. Xella-Hansen⁹, J. Yang⁴, Yu. Zaitsev²⁵, M. Zavertyaev^{15,38}, G. Zech³¹, T. Zeuner³¹, A. Zhelezov²⁵, Z. Zheng³, Z. Zhu³, R. Zimmermann³⁰, T. Živko¹⁹, A. Zoccoli⁶, J. Zweizig^{13,22}

¹ Department of Physics, University of Texas, Austin, TX 78712-1081, USA^a

² Department ECM, Faculty of Physics, University of Barcelona, E-08028 Barcelona, Spain

³ Institute for High Energy Physics, Beijing 100039, P.R. China

⁴ Institute of Engineering Physics, Tsinghua University, Beijing 100084, P.R. China

⁵ Institut für Physik, Humboldt-Universität zu Berlin, D-10115 Berlin, Germany

⁶ Dipartimento di Fisica dell' Università di Bologna and INFN Sezione di Bologna, I-40126 Bologna, Italy

⁷ Department of Physics, University of Cincinnati, Cincinnati, Ohio 45221, USA^a

⁸ LIP Coimbra and Lisboa, P-3004-516 Coimbra, Portugal

⁹ Niels Bohr Institutet, DK 2100 Copenhagen, Denmark

¹⁰ Department of Physics and Astronomy, Wayne State University, Detroit, MI 48202, USA^a

¹¹ Institut für Physik, Universität Dortmund, D-44227 Dortmund, Germany^c

¹² Northwestern University, Evanston, IL 60208, USA^a

¹³ DESY, D-22603 Hamburg, Germany

¹⁴ Institut für Experimentalphysik, Universität Hamburg, D-22761 Hamburg, Germany^c

¹⁵ Max-Planck-Institut für Kernphysik, D-69117 Heidelberg, Germany^c

¹⁶ Physikalisches Institut, Universität Heidelberg, D-69120 Heidelberg, Germany^c

¹⁷ Department of Physics, University of Houston, Houston, TX 77204, USA^a

¹⁸ Institute for Nuclear Research, Ukrainian Academy of Science, 03680 Kiev, Ukraine

¹⁹ J. Stefan Institute, 1001 Ljubljana, Slovenia

²⁰ University of Ljubljana, 1001 Ljubljana, Slovenia

²¹ University of Maribor, 2000 Maribor, Slovenia

²² University of California, Los Angeles, CA 90024, USA

²³ Lund University, S-22362 Lund, Sweden

²⁴ Lehrstuhl für Informatik V, Universität Mannheim, D-68131 Mannheim, Germany

²⁵ Institute of Theoretical and Experimental Physics, 117259 Moscow, Russia^g

²⁶ Joint Institute for Nuclear Research Dubna, 141980 Dubna, Moscow region, Russia

²⁷ Moscow Physical Engineering Institute, 115409 Moscow, Russia

²⁸ Max-Planck-Institut für Physik, Werner-Heisenberg-Institut, D-80805 München, Germany^c

²⁹ Dept. of Physics, University of Oslo, N-0316 Oslo, Norway

³⁰ Fachbereich Physik, Universität Rostock, D-18051 Rostock, Germany^c

³¹ Fachbereich Physik, Universität Siegen, D-057068 Siegen, Germany^c

³² Universiteit Utrecht/NIKHEF, 3584 CB Utrecht, The Netherlands

³³ NIKHEF, 1009 DB Amsterdam, The Netherlands^k

³⁴ DESY Zeuthen, D-15738 Zeuthen, Germany

³⁵ Physik-Institut, Universität Zürich, CH-8057 Zürich, Switzerland

³⁶ Brookhaven National Laboratory, Upton, NY 11973, USA

³⁷ visitor from Dipartimento di Energetica dell' Università di Firenze and INFN Sezione di Bologna, Italy

- ³⁸ visitor from P.N. Lebedev Physical Institute, 117924 Moscow B-333, Russia
³⁹ visitor from Moscow Physical Engineering Institute, 115409 Moscow, Russia
⁴⁰ visitor from Institute of Nuclear Power Engineering, 249030, Obninsk, Russia
⁴¹ visitor from Institute for High Energy Physics, Protvino, Russia
⁴² visitor from Institute for Nuclear Research, INRNE-BAS, Sofia, Bulgaria
⁴³ visitor from High Energy Physics Institute, 380086 Tbilisi, Georgia
⁴⁴ visitor from Yerevan Physics Institute, Yerevan, Armenia

^asupported by the U.S. Department of Energy (DOE)

^bsupported by the CICYT contract AEN99-0483

^csupported by the Bundesministerium für Bildung und Forschung, FRG, under contract numbers 05-7BU35I, 05-7DO55P, 05 HB1HRA, 05 HB1KHA, 05 HB1PEA, 05 HB1PSA, 05 HB1VHA, 05 HB9HRA, 05 7HD15I, 05 7HH25I, 05 7MP25I, 05 7SI75I

^dsupported by the Portuguese Fundação para a Ciência e Tecnologia

^esupported by the Danish Natural Science Research Council

^fsupported by the Texas Advanced Research Program

^gsupported by the National Academy of Science and the Ministry of Education and Science of Ukraine

^hsupported by the U.S. National Science Foundation Grant PHY-9986703

ⁱsupported by the Russian Fundamental Research Foundation under grant RFFI-00-15-96584 and the BMBF via the Max Planck Research Award

^jsupported by the Norwegian Research Council

^ksupported by the Foundation for Fundamental Research on Matter (FOM), 3502 GA Utrecht, The Netherlands

^lsupported by the Swiss National Science Foundation

Abstract

Inclusive differential cross sections $d\sigma_{pA}/dx_F$ and $d\sigma_{pA}/dp_t^2$ for the production of K_S^0 , Λ , and $\bar{\Lambda}$ particles are measured at HERA in proton-induced reactions on C, Al, Ti, and W targets. The incident beam energy is 920 GeV, corresponding to $\sqrt{s} = 41.6$ GeV in the proton-nucleon system. The ratios of differential cross sections $d\sigma_{pA}(K_S^0)/d\sigma_{pA}(\Lambda)$ and $d\sigma_{pA}(\bar{\Lambda})/d\sigma_{pA}(\Lambda)$ are measured to be 6.2 ± 0.5 and 0.66 ± 0.07 , respectively, for $x_F \approx -0.06$. No significant dependence upon the target material is observed. Within errors, the slopes of the transverse momentum distributions $d\sigma_{pA}/dp_t^2$ also show no significant dependence upon the target material. The dependence of the extrapolated total cross sections σ_{pA} on the atomic mass A of the target material is discussed, and the deduced cross sections per nucleon σ_{pN} are compared with results obtained at other energies.

Key words: Hyperons, cross section, A-dependence

PACS: 13.85.-t 13.85.Ni 13.85.Lg

1 Introduction

We present measurements of inclusive production cross sections for K_S^0 , Λ , and $\bar{\Lambda}$ particles, collectively referred to as V^0 particles, in collisions of 920 GeV protons with several nuclear targets of different atomic mass A . The production of V^0 particles has been studied by numerous experiments with different beams (π , K , p , n , Σ^-) on different targets, covering a momentum range of 4–400 GeV/ c (see [1, 2, 3, 4, 5, 6, 7, 8, 9, 10, 11, 12, 13, 14, 15, 16, 17, 18, 19, 20] and refs. therein). A large fraction of these experiments utilized bubble chambers. At center-of-mass energies above $\sqrt{s} \approx 30$ GeV, inclusive V^0 production cross sections have been measured by experiments at the CERN proton-proton Intersecting Storage Rings (ISR) [21, 22, 23, 24]. However, only a lower limit for the $\bar{\Lambda}$ cross section has been reported [22]. Also, the V^0 total production cross sections reported in [24] are substantially above expectations based on extrapolation of results obtained at lower energies.

Recently, progress in heavy ion physics has renewed interest in studies of strange-particle production. One of the main goals of heavy-ion experiments is the observation of the quark-gluon plasma [26], and one of the signatures for this new state is enhanced production of strange particles [27]. Observables of interest are ratios of antibaryons to baryons at mid-rapidity, which are important for net baryon density evaluations and which have been used recently to extract values of chemical potentials and temperatures [28, 29] for Au-Au collisions at RHIC. Also of interest are the squared transverse momentum (p_t^2) distributions, $d\sigma/dp_t^2$, which contain information about the temperature of the system; specifically, if it reached thermal equilibrium (see, e.g., [30]). These investigations attach importance to a comprehensive measurement of strange-particle production properties in “ordinary” nucleon-nucleon (NN) and nucleon-nucleus (NA) collisions. The latter are expected to establish a valuable baseline for comparisons among AA results [28].

2 The HERA-B Experiment

HERA-B is a fixed target experiment at the 920 GeV proton storage ring of HERA at DESY [31]. It was originally designed to study CP violation in $B^0 \rightarrow J/\psi K_S^0$ decays; thus, the spectrometer was optimized to detect and precisely locate decays of J/ψ and longer-lived K_S^0 mesons. The first experience with the apparatus was gained during an engineering run in the year 2000. While the main goal was to commission the sophisticated J/ψ -based trigger system, there were also run periods dedicated to recording minimum bias events, i.e., events selected with a random trigger that uniformly sampled all HERA bunches. These data allow for precise measurements of strange-particle production cross sections.

A plan view of the HERA-B spectrometer is shown in Fig. 1. The spectrometer dipole magnet provides a field integral of 2.13 T-m, with the main component perpendicular to the x - z plane. The apparatus (including particle identification counters) has a forward acceptance of 10–220 mrad in the bending plane and 10–160 mrad in the non-bending plane. The experiment uses a multi-wire fixed target which operates in the halo of the proton beam during HERA e - p collider operation. Up to eight different targets can be operated simultaneously, with their positions being adjusted dynamically in order to maintain a constant interaction rate between 1 and 40 MHz. For the measurements presented here, wires made of carbon (C), aluminum (Al), titanium (Ti), and tungsten (W) were used. Their transverse width was 50 μm , and their thickness along the beam direction was 1000 μm for carbon and 500 μm otherwise.

The tracking system consists of a vertex detector system (VDS) and a main tracker system. The latter is separated into an inner tracker (ITR) close to the proton beam-pipe and an outer tracker (OTR) farther out. The VDS [32] features 64 double-sided silicon microstrip detectors arranged in eight stations along, and four quadrants around, the proton beam. The silicon strips have a readout pitch of approximately 50 μm . The strips are rotated on the wafer such that each pair of wafers provides four stereo views: $\pm 2.5^\circ$ and $90^\circ \pm 2.5^\circ$. The ITR uses GEM microstrip gas chambers [33], and the OTR uses honeycomb drift chambers [34]. There are a total of 13 ITR + OTR tracking stations, with each one referred to as a “superlayer.” For the analysis presented here, only data from the six superlayers located downstream of the magnet are used. Also, this analysis does not use particle-identification information from the ring-imaging Cherenkov counter [35], the electromagnetic calorimeter [36], or the muon detector [37].

3 Data Analysis

The results presented here are based on a sample of ~ 2.4 million randomly triggered events recorded in April 2000. The HERA proton beam had 180 filled bunches and a bunch crossing rate of 10.4 MHz. The interaction rate was adjusted to values between 2 and 6 MHz, leading to most bunch crossings ($\geq 90\%$) having either 0 or 1 interaction. For this analysis, only tracks with a minimum of five hits in the VDS and ten hits in the main tracker were used. The same event selection procedures were applied as were used to determine the integrated luminosity. No explicit selection on track multiplicity was applied.

In each event with at least two tracks, a full combinatorial search for V^0 candidates was performed. V^0 candidates were selected from all pairs of oppositely charged tracks that formed a vertex downstream of the primary vertex. The minimum distance between the two tracks was required to be less than 0.7 mm. No particle identification criteria were applied to the tracks. The primary vertex was determined from all tracks reconstructed in the VDS excluding the V^0 tracks. Using tracks reconstructed in both the VDS and the main tracker, we measured the spatial resolution of the reconstructed primary vertex to be 0.7 mm along the z -direction. The position of the primary vertex was required to coincide with the center of a target wire to within three standard deviations (2.1 mm). If a primary vertex could not be reconstructed, the z coordinate of the target was used to calculate the z -component of the particle's flight length. An Armenteros-Podolanski plot [39] for the selected V^0 candidates is shown in Fig. 2. Clusters of events shaped according to the kinematics of $K_S^0 \rightarrow \pi^+ \pi^-$, $\Lambda \rightarrow p \pi^-$ and $\bar{\Lambda} \rightarrow \bar{p} \pi^+$ decays are clearly visible. The V^0 candidates from those regions of Fig. 2 in which two of the three V^0 species overlap – and thus are kinematically indistinguishable – were rejected. This reduced the K_S^0 yield by 3.5% and the Λ ($\bar{\Lambda}$) yield by 10% (20%). An additional requirement $\tilde{p}_t \cdot c\tau > 0.05$ (GeV/c) \cdot cm was applied to reduce background from $\gamma \rightarrow e^+e^-$ conversions, where \tilde{p}_t is the transverse momentum relative to the V^0 line-of-flight and τ is the V^0 proper lifetime. This requirement also reduced combinatorial background from the target, which populates the lower region of Fig. 2.

The invariant mass distributions for the selected candidates are shown in Fig. 3. Clear signals corresponding to K_S^0 , Λ , and $\bar{\Lambda}$ particles are visible. In order to estimate the event yields, fits with a Gaussian function for signal and a third-order Legendre polynomial for background were performed. The width obtained for the K_S^0 mass peak was about $5.6 \text{ MeV}/c^2$, which is consistent with the momentum resolution of $\sigma(p)/p^2 \approx 10^{-4} \text{ (GeV}/c)^{-1}$. The resultant event yields are summarized in Table 1 for each target material.

4 Acceptance Determination

A Monte Carlo (MC) simulation is used to determine the reconstruction efficiency for the selected particles and decay channels. The production of a V^0 particle in an inelastic event is simulated using a kinematic distribution of the form:

$$\frac{d^2\sigma}{dp_t^2 dx_F} = C \cdot (1 - |x_F|)^n \cdot \exp(-B \cdot p_t^2), \quad (1)$$

where x_F is the Feynman- x variable and p_t the transverse momentum in the laboratory system. This phenomenological ansatz is motivated by quark counting rules and phase space arguments [40] and has been shown to describe a substantial amount of data well (see [20] and refs. therein). The value of the parameter B of $2.1 \text{ (GeV}/c)^{-2}$ is taken from Ref. [20], and a flat x_F distribution is assumed ($n=0$). The x_F bin size of 0.015 is chosen to be compatible with the momentum resolution. After the generation of the V^0 particle, the remaining momentum is assigned to a virtual π^+ , which is input as a beam particle to the FRITIOF 7.02 package [44] in order to further simulate interactions within the nucleus.

The generated particles are propagated through the geometry and material description of the detector using the GEANT 3.21 package [45]. The detector response is simulated including realistic descriptions of chamber efficiencies and dead channels. The MC events are subjected to the same reconstruction chain as that used for the data. For tracks within the geometrical acceptance that originate from V^0 decays, we determine an efficiency of $\sim 90\%$ to reconstruct the track and assign a momentum. This value is confirmed by the analysis of real data.

After all cuts, the efficiency to identify a V^0 particle is approximately 10% for K_S^0 and 5% for Λ and $\bar{\Lambda}$. These values are dominated by the geometrical acceptance. All efficiencies are computed in bins of rapidity y and p_t^2 in order to be independent of the details of the MC model of V^0 production.

5 Production Cross Sections

The cross section $\Delta\sigma_{V^0}$ for the production of a V^0 particle within the spectrometer acceptance can be expressed as:

$$\Delta\sigma_{V^0} = \frac{1}{B_{V^0} \mathcal{L}} \iint_{accp} \frac{N_{V^0}(y, p_t^2)}{\varepsilon(y, p_t^2)} dy \cdot dp_t^2, \quad (2)$$

where $N_{V^0}(y, p_t^2)$ is the number of V^0 candidates observed in bins of rapidity y and p_t^2 . The detection efficiency $\varepsilon(y, p_t^2)$ is calculated from the MC simulations described above. The branching fraction B_{V^0} for the detected decay $V^0 \rightarrow f$ is taken from Ref. [43]. Finally, the integrated luminosity \mathcal{L} is computed from the interaction rate at the target [38]. The resultant luminosities for each target material are listed in Table 1.

The efficiency-corrected values of the inclusive differential cross section $d\sigma_{pA}/dx_F$ for V^0 production within the spectrometer acceptance are listed in Table 2 for the various target materials. The corresponding x_F interval is $[-0.12, 0]$, except in the case of K_S^0 production on the W target, where it is $[-0.09, 0]$.

As the x_F acceptance of the spectrometer is restricted, for comparison with results from other experiments it is necessary to extrapolate the differential cross sections $d\sigma_{pA}/dx_F$ to the entire kinematic range $x_F \in [-1, +1]$. This was done using the parameterization $d\sigma/dx_F \propto (1 - |x_F|)^n$, where n is a constant. The values used for n are taken from previous measurements of inclusive strange-particle production [20] and are listed in Table 2. The difference between values for different V^0 species is compatible with theoretical predictions based upon quark counting rules [40]. The resulting V^0 total production cross sections (σ_{pA}) are also listed in Table 2. The fraction of the cross sections within the detector acceptance is 30% for K_S^0 ($n = 6.0$), 17% for Λ ($n = 2.2$), and 34% for $\bar{\Lambda}$ ($n = 8.0$).

The dependence of the measured cross sections on the atomic mass of the target material is shown in Fig. 4 along with fits of two different kinds. The dashed lines are fits to the form $\sigma_{pA} \propto A^\alpha$, while the solid lines are fits within the framework of the Glauber model [41]. These latter fits allow us to extract the production cross section per nucleon, σ_{pN} . All fit results are listed in Table 3. The Glauber model calculations use a nucleon density given by the Saxon-Woods potential [42], and the total cross sections for KN and ΛN collisions and the slope of the diffraction scattering cone are taken from Refs. [42, 43].

5.1 The p_t^2 Differential Cross Sections

The extrapolation of the the p_t^2 distributions for K_S^0 , Λ , and $\bar{\Lambda}$ particles over the entire x_F range $[-1, +1]$ yields the differential cross sections $d\sigma/dp_t^2$ listed in Table 4. These data are presented graphically in Fig. 5 together with fits to the form

$$\frac{d\sigma}{dp_t^2} = \sigma \cdot B \cdot \exp(-B \cdot p_t^2), \quad (3)$$

where the parameter B is independent of x_F and p_t^2 . Table 5 summarizes the values of B obtained for the different target materials and V^0 particles. No significant dependence upon the target material is seen.

5.2 Systematic Uncertainties

To estimate the uncertainty in the efficiency determination, we varied the V^0 selection criteria applied to data and simulated events. Different track quality requirements used in the vertex reconstruction were studied in order to understand differences observed between data and MC results; the variation of cuts causes a change of 7% in the cross section values. Cuts on the primary and V^0 vertices give a 2% change. The variation of the distance required between tracks to form a V^0 decay vertex contributes another 2%. The systematic error due to the limited statistics of MC events is 1% for K_S^0 and 3% for Λ and $\bar{\Lambda}$ particles. The use of different fitting functions for the shape of the background in the invariant mass spectra, and the variations of bin sizes for invariant mass, x_F , and p_t^2 , result in a change in the cross sections of approximately 5%.

The efficiency of the ITR improved during data taking (as this system was further commissioned), and this caused a systematic shift in the track reconstruction efficiencies. These shifts are +14%, +11%, and +20% for K_S^0 , Λ , and $\bar{\Lambda}$ particles, respectively.

We used three independent methods to determine the integrated luminosity. The results differ by 4–7%, which we include as an additional systematic uncertainty. For more details, see Ref. [38].

To extrapolate $d\sigma/dp_t^2$ to the entire kinematic range of x_F , we used Eq. 1 with experimentally determined values [20] of the parameter n . Varying this parameter by the estimated experimental uncertainty (± 0.5) leads to a variation of 5% in the K_S^0 cross sections, 12% in the Λ cross sections, and 2% in the $\bar{\Lambda}$ cross sections.

The cross sections were measured on different nuclei, and extracting the cross sections per nucleon (σ_{pN}) from the measured values was done via the Glauber model. Variations of the parameters of this model give a 12% systematic uncertainty in σ_{pN} .

Adding all systematic errors in quadrature, we obtain the total systematic errors for the cross sections per nucleus $d\sigma_{pA}/dx_F$, $d\sigma_{pA}/dp_t^2$, and σ_{pA} , and for the cross section per nucleon σ_{pN} . All systematic errors are given in Tables 2, 3, and 4 (listed after statistical errors); the errors are asymmetric due to changes in running conditions for the ITR.

6 Discussion of Results

More precise than the production cross sections themselves are cross section ratios, since, for these, acceptance corrections and systematic errors to a large extent cancel. From the measurements presented above we calculate the ratios $d\sigma(K_S^0)/d\sigma(\Lambda) = 6.2 \pm 0.5$ and $d\sigma(\bar{\Lambda})/d\sigma(\Lambda) = 0.66 \pm 0.07$, for $x_F \approx -0.06$ (i.e., mid-rapidity). The $d\sigma(\bar{\Lambda})/d\sigma(\Lambda)$ ratio is plotted in Fig. 6 for the different target materials; no significant dependence upon the target material (i.e., atomic mass A) is seen, and this holds also for the $d\sigma(K_S^0)/d\sigma(\Lambda)$ ratio.

Ratios between antiparticle yields and particle yields measured at mid-rapidity have attracted special interest in studies of the dependence of AA collision dynamics upon collision energy [28, 29]. Fig. 6 shows the ratio of yields for $\bar{\Lambda}$ and Λ particles at mid-rapidity in AA collisions as a function of center-of-mass energy $\sqrt{s_{NN}}$. The data plotted are from the BNL AGS ($\sqrt{s_{NN}} \approx 5.4$ GeV), the CERN SPS ($\sqrt{s_{NN}} \approx 10$ –30 GeV), and RHIC ($\sqrt{s_{NN}} = 130$ GeV) [46, 47, 48, 49, 50, 51, 52]. Comparing these measurements with corresponding results from pp [7, 17, 46] and pA [46, 47, 48] collisions shows these data to exhibit a similar energy dependence, and the HERA-B result at $\sqrt{s} = 41.6$ GeV is consistent with this trend. Closer inspections suggests that the pp , pA , and AA data follow individual curves that are slightly shifted in energy. This would be consistent with results from NA49 [46], which found that in pp collisions at $\sqrt{s_{NN}} = 17.3$ GeV the ratio $d\sigma(\bar{\Lambda})/d\sigma(\Lambda)$ is about 60% larger than that in pA collisions, and in AA collisions at the same $\sqrt{s_{NN}}$ the ratio is about 60% smaller. However, more data are needed to confirm this behavior.

The measured p_t^2 spectra presented above are well-parametrized by Eq. 3. The results (Table 5) show no significant dependence upon the target material, and they are compatible with results from other experiments, e.g. from pp collisions at $\sqrt{s} = 27.6$ GeV, where at $p_t^2 < 1.5$ (GeV/c)² B parameters for K_S^0 , Λ and $\bar{\Lambda}$ particles of 3.59 ± 0.18 (GeV/c)⁻², 2.73 ± 0.21 (GeV/c)⁻² and 2.66 ± 0.74 (GeV/c)⁻², respectively, have been extracted [18]; for more examples see the compilation in [20]. Due to the limited statistics available, the present study was done in the p_t^2 region below 1.1 (GeV/c)²; thus we cannot confirm the flattening of the p_t^2 spectrum above 1.2 (GeV/c)² (see e.g. [17]).

The narrow acceptance in x_F for this data set also precludes us from measuring “leading particle” effects, which have been observed by other fixed target experiments at $x_F > 0.4$ (see e.g. [20, 53]). However, we have measured for the first time V^0 differential cross sections for different target materials at negative x_F ($-0.12 < x_F < 0$). We extrapolate these results to the full x_F range to obtain total cross sections for different values of atomic mass A . We fit these values to the conventional expression $\sigma_{pA} \propto A^\alpha$ and also to the Glauber model. The values obtained for α from the first fit (Table 3) are very similar to those observed in other hadroproduction processes, which can be characterized [54] by $\alpha(x_F) = 0.8 - 0.75 x_F + 0.45 x_F^3/|x_F|$.

From the Glauber-model fits we extract V^0 cross sections per nucleon, σ_{pN} (Table 3). Fig. 7 presents a comparison of these results with previous experimental results [6, 7, 8, 9, 10, 11, 12, 13, 14, 15, 16, 17, 18, 19, 20, 21, 22, 23, 24]. The HERA-B results show good agreement with the general systematic trend as quantified by the curves. These curves were calculated from a fit [18] for the average number of V^0 particles per inelastic collision as a function of $\ln(s)$, in the interval $13.5 < \sqrt{s} < 28$ GeV. The data in Fig. 7 suggest that this parametrization is valid up to the HERA-B energy of $\sqrt{s} = 41.6$ GeV, and even up to the highest ISR energy of $\sqrt{s} = 63$ GeV. Our value for the K_S^0 cross section is in good agreement with the value obtained at $\sqrt{s} = 52.5$ GeV [23]. The large cross section reported in [24] for $\sqrt{s} = 63$ GeV has been recognized [25]

to be biased by ghost tracks. In addition, our value for the Λ total cross section per nucleon is in good agreement with the values obtained at the ISR at $\sqrt{s}=53$ GeV and $\sqrt{s}=62$ GeV [22]. As Λ production is known to receive large contributions from fragmentation processes, such a good agreement is noteworthy: it implies that also for small x_F the parameterization of the (double-differential) cross section given in Eq. 1 is valid.

Acknowledgments

We express our gratitude to the DESY laboratory for the strong support in setting up and running the HERA-B experiment. We are also indebted to the DESY accelerator group for the continuous efforts to provide good and stable beam conditions. The HERA-B experiment would not have been possible without the enormous effort and commitment of our technical and administrative staff. It is a pleasure to thank all of them.

We thank the theoreticians B. Kopeliovich and H.J. Pirner for many stimulating discussions and suggestions.

References

- [1] N. N. Biswas *et al.*, Nucl. Phys. **B167** (1980) 41.
- [2] S. Mikocki *et al.*, Phys. Rev. **D34** (1986) 42.
- [3] D. Ljung *et al.*, Phys. Rev. **D15** (1977) 3163.
- [4] D. Bogert *et al.*, Phys. Rev. **D16** (1977) 2098.
- [5] R. T. Edwards *et al.*, Phys.Rev. **D18** (1978) 76.
- [6] B. Y. Oh *et al.*, Nucl. Phys. **B49** (1972) 13.
- [7] V. Blobel *et al.*, Nucl. Phys. **B69** (1974) 454.
- [8] K. Jaeger *et al.*, Phys. Rev. **D11** (1975) 1756.
- [9] H. Bøggild *et al.*, Nucl. Phys. **B57** (1973) 77.
- [10] M. Alston-Garnjost *et al.*, Phys. Rev. Lett. **35** (1975) 142.
- [11] J. W. Chapman *et al.*, Phys. Lett. **47B** (1973) 465.
- [12] K. Jaeger *et al.*, Phys. Rev. **D11** (1975) 2405.
- [13] A. Sheng *et al.*, Phys. Rev. **D11** (1975) 1733.
- [14] K. Heller *et al.*, Phys. Rev. **D16** (1977) 2737.
- [15] P. Skubic *et al.*, Phys. Rev. **D18** (1978) 3115.
- [16] F. T. Dao *et al.*, Phys. Rev. Lett. **30** (1973) 1151.
- [17] M. Asai *et al.*, Z. Phys. **C27** (1985) 11.
- [18] H. Kichimi *et al.*, Phys. Rev. **D20** (1979) 37.
- [19] A. Aleev *et al.*, Yad. Fiz. **44** (1986) 661;
Sov. J. Nucl. Phys. **44**(3) (1986) 429.
- [20] M. I. Adamovich *et al.*, Eur. J. Phys., in print
DOI 10.1140/epjc/s2002-01073-6.

- [21] F. W. Büsler *et al.*, Phys. Lett. **61B** (1976) 309.
- [22] S. Erhan *et al.*, Phys. Lett. **85B** (1979) 447.
- [23] D. Drijard *et al.*, Z. Phys. **C9** (1981) 293.
- [24] D. Drijard *et al.*, Z. Phys. **C12** (1982) 217.
- [25] J. Spengler and D. Wegener, private communication, 2002.
- [26] see, e.g., Proc. 15th Int. Conf. on Ultra-Relativistic Nucleus-Nucleus Collisions (QM2001), Nucl. Phys. **A698** (2002) Issue 1-4.
- [27] S. A. Bass *et al.*, Nucl. Phys. **A661** (1999) 205c.
- [28] J. Rafelski *et al.*, nucl-th/0104042.
- [29] P. Braun-Munzinger *et al.* nucl-ph/0105229.
- [30] L. V. Bravina *et al.*, Phys. Rev. **C60** (1999) 024904.
- [31] E. Hartouni *et al.*, HERA-B Design Report, DESY-PRC 95/01 (1995).
- [32] C. Bauer *et al.*, Nucl. Instr. Methods **A453** (2000) 103.
- [33] T. Zeuner, Nucl. Instr. Methods **A446** (2000) 324.
- [34] M. Capeans, Nucl. Instr. Methods **A446** (2000) 317.
- [35] J. Pyrlik, Nucl. Instr. Methods **A446** (2000) 299.
- [36] A. Zoccoli, Nucl. Instr. Methods **A446** (2000) 246.
- [37] A. Arefiev *et al.*, IEEE Trans. Nucl. Sci. **48** (2001) 1059.
- [38] HERA-B collaboration, “Luminosity Measurement at HERA-B,” to be published.
- [39] J. Podolansky and R. Armenteros, Phil. Mag. **45** (1954) 13.
- [40] S. J. Brodsky *et al.*, Phys. Rev. **D17** (1978) 848, and J. F. Gunion, Phys. Lett. **88B** (1979) 150, and refs. therein.
- [41] R. J. Glauber *et al.*, Lectures in Theoretical Physics, Vol. 1, (Interscience Publishers, New York, 1959).
- [42] S. P. Denisov *et al.*, Nucl. Phys. **B61** (1973) 62.
- [43] The Particle Data Group, Eur. J. Phys., **C15** (2000) 1.
- [44] B. Andersson *et al.*, Z. Phys. **C57** (1993) 485-494;
H. Pi, Comput. Phys. Commun. **71** (1992) 173-192.
- [45] GEANT 3.21, CERN Program Library W5103, CERN 1993.
- [46] K. Kadija *et al.* (NA49 collaboration), J. Phys. G: Nucl. Part. Phys. **28** (2002) 1675.
- [47] K. Fanebust *et al.* (NA57 collaboration), J. Phys. G: Nucl. Part. Phys. **28** (2002) 1607.
- [48] R. Caliendo *et al.*, J. Phys. G: Nucl. Part. Phys. **25** (2002) 171.
- [49] B.A. Cole *et al.* (E802 collaboration), Nucl. Phys. **A590** (1995) 179c.

- [50] A. Mischke *et al.* (NA49 collaboration), nucl-ex/0209002.
- [51] K. Adcox *et al.* (PHENIX collaboration), nucl-ex/0204007.
- [52] C. Adler *et al.* (STAR collaboration), nucl-ex/0203016.
- [53] M. Basile *et al.*, Nuovo Cim. **66A** (1981) 129.
- [54] W. M. Geist, Nucl. Phys. **A525** (1991) 149c.

Table 1: Integrated luminosities \mathcal{L}_A in mb^{-1} for the indicated targets of atomic mass A [38], and the corresponding numbers of events $N(\text{evt})$ and V^0 particles $N(V^0)$ obtained. Uncertainties listed for \mathcal{L}_A are systematic; those listed for $N(V^0)$ are statistical.

| | C | Al | Ti | W |
|---------------------------------|---------------|---------------|---------------|--------------|
| A | 12 | 27 | 48 | 184 |
| $\mathcal{L}_A \cdot \text{mb}$ | 1093 ± 38 | 1030 ± 67 | 308 ± 10 | 47 ± 3 |
| $N(\text{evt})$ | 496694 | 893885 | 467943 | 512897 |
| $N(K_S^0)$ | 2566 ± 58 | 4398 ± 81 | 2022 ± 52 | 909 ± 40 |
| $N(\Lambda)$ | 512 ± 31 | 831 ± 43 | 412 ± 27 | 224 ± 24 |
| $N(\bar{\Lambda})$ | 241 ± 24 | 503 ± 41 | 222 ± 23 | 144 ± 22 |

Table 2: The inclusive differential cross sections $d\sigma_{pA}/dx_F$ in mb measured in the x_F interval $[-0.12, 0]$ for the production of K_S^0 , Λ , and $\bar{\Lambda}$ particles on indicated targets. Also listed are the total cross sections σ_{pA} obtained by extrapolation to the full x_F range (see text). Values are followed by statistical and systematic errors. The values of the parameter n used for the extrapolations (see Eq. 1) are also given. The x_F interval for the case of K_S^0 production on the W target is $[-0.09, 0]$.

| | Trgt | n | $d\sigma_{pA}/dx_F$ (mb) | σ_{pA} (mb) |
|-----------------|------|-----|---|--|
| K_S^0 | C | 6.0 | $215. \pm 12. \begin{smallmatrix} +33. \\ -13. \end{smallmatrix}$ | $86. \pm 5. \begin{smallmatrix} +14. \\ -7. \end{smallmatrix}$ |
| | Al | | $429. \pm 33. \begin{smallmatrix} +68. \\ -34. \end{smallmatrix}$ | $174. \pm 13. \begin{smallmatrix} +30. \\ -16. \end{smallmatrix}$ |
| | Ti | | $612. \pm 33. \begin{smallmatrix} +92. \\ -37. \end{smallmatrix}$ | $248. \pm 13. \begin{smallmatrix} +40. \\ -20. \end{smallmatrix}$ |
| | W | | $2044. \pm 167. \begin{smallmatrix} +322. \\ -156. \end{smallmatrix}$ | $761. \pm 63. \begin{smallmatrix} +129. \\ -68. \end{smallmatrix}$ |
| Λ | C | 2.2 | $53. \pm 4. \begin{smallmatrix} +7. \\ -3. \end{smallmatrix}$ | $38. \pm 3. \begin{smallmatrix} +6. \\ -5. \end{smallmatrix}$ |
| | Al | | $90. \pm 8. \begin{smallmatrix} +13. \\ -8. \end{smallmatrix}$ | $64. \pm 6. \begin{smallmatrix} +12. \\ -9. \end{smallmatrix}$ |
| | Ti | | $163. \pm 13. \begin{smallmatrix} +21. \\ -13. \end{smallmatrix}$ | $115. \pm 20. \begin{smallmatrix} +20. \\ -15. \end{smallmatrix}$ |
| | W | | $558. \pm 62. \begin{smallmatrix} +78. \\ -45. \end{smallmatrix}$ | $399. \pm 47. \begin{smallmatrix} +76. \\ -56. \end{smallmatrix}$ |
| $\bar{\Lambda}$ | C | 8.0 | $32. \pm 3. \begin{smallmatrix} +7. \\ -2. \end{smallmatrix}$ | $11. \pm 1. \begin{smallmatrix} +2.3 \\ -0.7 \end{smallmatrix}$ |
| | Al | | $69. \pm 8. \begin{smallmatrix} +15. \\ -6. \end{smallmatrix}$ | $25. \pm 3. \begin{smallmatrix} +5.3 \\ -2.7 \end{smallmatrix}$ |
| | Ti | | $96. \pm 11. \begin{smallmatrix} +20. \\ -6. \end{smallmatrix}$ | $34. \pm 4. \begin{smallmatrix} +7.5 \\ -2.7 \end{smallmatrix}$ |
| | W | | $375. \pm 58. \begin{smallmatrix} +83. \\ -33. \end{smallmatrix}$ | $131. \pm 20. \begin{smallmatrix} +29. \\ -10. \end{smallmatrix}$ |

Table 3: The V^0 production cross sections per nucleon (σ_{pN}) in mb with statistical and systematic errors, and the values of α resulting from fitting the cross sections per nucleus to the form $\sigma_{pA} \propto A^\alpha$. For the values of α , the errors listed are statistical only.

| | K_S^0 | Λ | $\bar{\Lambda}$ |
|--------------------|--|--|--|
| σ_{pN} (mb) | $9.0 \pm 0.3 \begin{smallmatrix} +1.8 \\ -1.3 \end{smallmatrix}$ | $4.3 \pm 0.2 \begin{smallmatrix} +0.9 \\ -0.7 \end{smallmatrix}$ | $1.4 \pm 0.1 \begin{smallmatrix} +0.3 \\ -0.2 \end{smallmatrix}$ |
| α | 0.78 ± 0.04 | 0.85 ± 0.05 | 0.82 ± 0.07 |

Table 4: The inclusive differential cross sections $d\sigma_{pA}/dp_t^2$ in $\text{mb}/(\text{GeV}/c)^2$ for the production of V^0 particles on indicated targets as obtained from extrapolation to the full x_F range. Values are followed by statistical and systematic errors. The p_t^2 bins (Δp_t^2) are in $(\text{GeV}/c)^2$; the p_t resolution is 1.7 MeV/c. Because of limited statistics, no cross sections are given for the production of $\bar{\Lambda}$ particles on the W target.

| Δp_t^2 | C | Al | Ti | W |
|-----------------|------------------------------|------------------------------|------------------------------|----------------------------------|
| K_S^0 | | | | |
| 0.0 – 0.2 | $230. \pm 20._{-18.}^{+37.}$ | $454. \pm 54._{-41.}^{+77.}$ | $619. \pm 53._{-50.}^{+99.}$ | $1901. \pm 254._{-171.}^{+323.}$ |
| 0.2 – 0.4 | $94. \pm 10._{-8.}^{+15.}$ | $191. \pm 28._{-17.}^{+32.}$ | $275. \pm 29._{-22.}^{+44.}$ | $899. \pm 141._{-81.}^{+153.}$ |
| 0.4 – 0.6 | $49. \pm 7._{-4.}^{+8.}$ | $101. \pm 19._{-9.}^{+17.}$ | $156. \pm 20._{-12.}^{+25.}$ | $560. \pm 92._{-50.}^{+95.}$ |
| 0.6 – 0.8 | $28. \pm 5._{-2.}^{+4.}$ | $64. \pm 14._{-5.}^{+11.}$ | $99. \pm 15._{-8.}^{+16.}$ | $229. \pm 57._{-21.}^{+39.}$ |
| 0.8 – 1.0 | $18. \pm 4._{-1.}^{+3.}$ | $33. \pm 10._{-3.}^{+6.}$ | $51. \pm 11._{-4.}^{+8.}$ | $146. \pm 47._{-13.}^{+25.}$ |
| 1.0 – 1.2 | $14. \pm 3._{-1.}^{+2.}$ | $29. \pm 10._{-3.}^{+5.}$ | $42. \pm 10._{-3.}^{+7.}$ | $75. \pm 34._{-7.}^{+13.}$ |
| Λ | | | | |
| 0.0 – 0.2 | $58. \pm 11._{-8.}^{+10.}$ | $103. \pm 23._{-14.}^{+20.}$ | $91. \pm 34._{-12.}^{+15.}$ | $677. \pm 200._{-95.}^{+129.}$ |
| 0.2 – 0.4 | $53. \pm 6._{-7.}^{+9.}$ | $78. \pm 11._{-11.}^{+15.}$ | $167. \pm 20._{-22.}^{+28.}$ | $327. \pm 81._{-46.}^{+62.}$ |
| 0.4 – 0.6 | $32. \pm 4._{-4.}^{+5.}$ | $54. \pm 8._{-8.}^{+10.}$ | $94. \pm 13._{-12.}^{+16.}$ | $364. \pm 60._{-51.}^{+69.}$ |
| 0.6 – 0.8 | $17. \pm 3._{-2.}^{+3.}$ | $33. \pm 5._{-5.}^{+6.}$ | $70. \pm 10._{-9.}^{+12.}$ | $249. \pm 45._{-35.}^{+47.}$ |
| 0.8 – 1.0 | $15. \pm 3._{-2.}^{+3.}$ | $27. \pm 5._{-4.}^{+5.}$ | $57. \pm 10._{-7.}^{+10.}$ | $263. \pm 45._{-37.}^{+50.}$ |
| 1.0 – 1.2 | $8. \pm 2._{-1.}^{+1.}$ | $14. \pm 3._{-2.}^{+3.}$ | $44. \pm 8._{-6.}^{+7.}$ | $120. \pm 31._{-17.}^{+23.}$ |
| $\bar{\Lambda}$ | | | | |
| 0.0 – 0.2 | $19. \pm 5._{-1.}^{+4.}$ | $49. \pm 11._{-4.}^{+11.}$ | $71. \pm 17._{-6.}^{+16.}$ | – |
| 0.2 – 0.4 | $16. \pm 2._{-1.}^{+3.}$ | $29. \pm 4._{-2.}^{+6.}$ | $29. \pm 6._{-2.}^{+6.}$ | – |
| 0.4 – 0.6 | $8. \pm 1._{-0.5}^{+1.6}$ | $16. \pm 3._{-1.}^{+4.}$ | $28. \pm 4._{-2.}^{+6.}$ | – |
| 0.6 – 0.8 | $5. \pm 1._{-0.3}^{+1.}$ | $16. \pm 2._{-1.}^{+4.}$ | $20. \pm 4._{-2.}^{+4.}$ | – |
| 0.8 – 1.0 | $4.6 \pm 0.9_{-0.3}^{+1.}$ | $10. \pm 2._{-0.8}^{+2.}$ | $10. \pm 3._{-1.}^{+2.}$ | – |
| 1.0 – 1.2 | $2.4 \pm 0.7_{-0.1}^{+0.5}$ | $5. \pm 1._{-0.4}^{+1.}$ | $9. \pm 2._{-1.}^{+2.}$ | – |

Table 5: The values of the parameter B obtained by fitting the differential cross section to the form $d\sigma/dp_t^2 \propto \exp(-B \cdot p_t^2)$, together with fit errors. Because of limited statistics, no value is obtained for $\bar{\Lambda}$ particles produced on the W target.

| | $B (\text{GeV}/c)^{-2}$ | | | |
|-----------------|-------------------------|---------------|---------------|---------------|
| | C | Al | Ti | W |
| K_S^0 | 3.3 ± 0.2 | 3.2 ± 0.3 | 3.0 ± 0.2 | 3.3 ± 0.3 |
| Λ | 2.3 ± 0.3 | 2.0 ± 0.3 | 1.7 ± 0.3 | 1.3 ± 0.5 |
| $\bar{\Lambda}$ | 2.2 ± 0.3 | 2.0 ± 0.3 | 1.8 ± 0.3 | – |

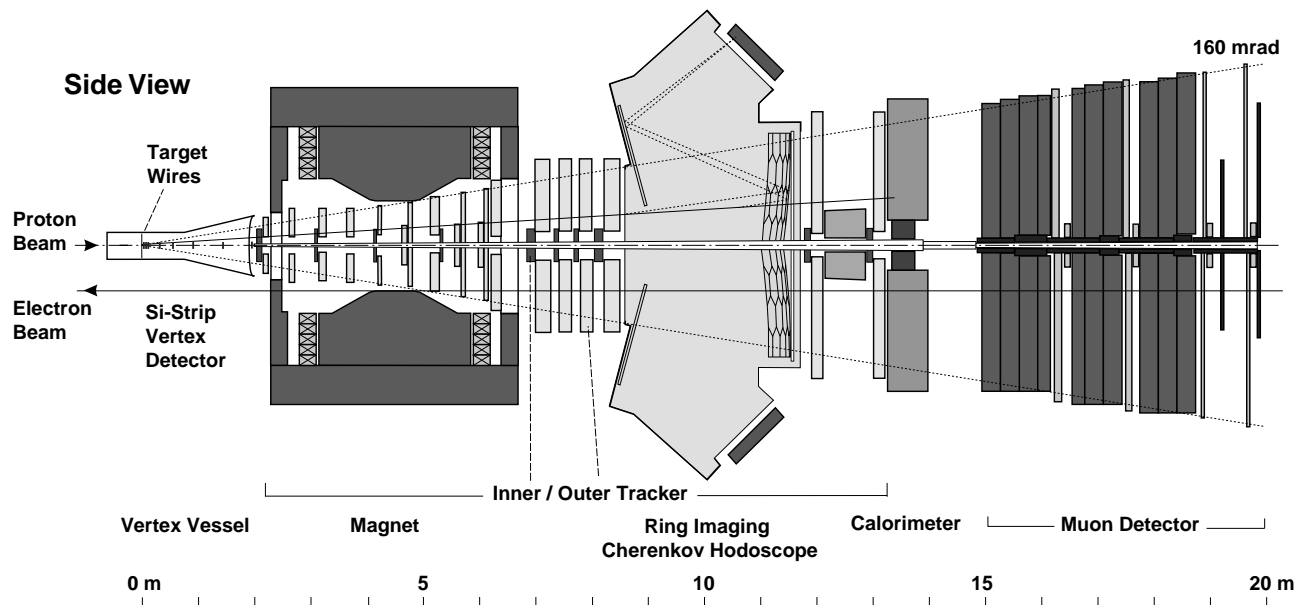


Figure 1: Plan view of the HERA-B detector.

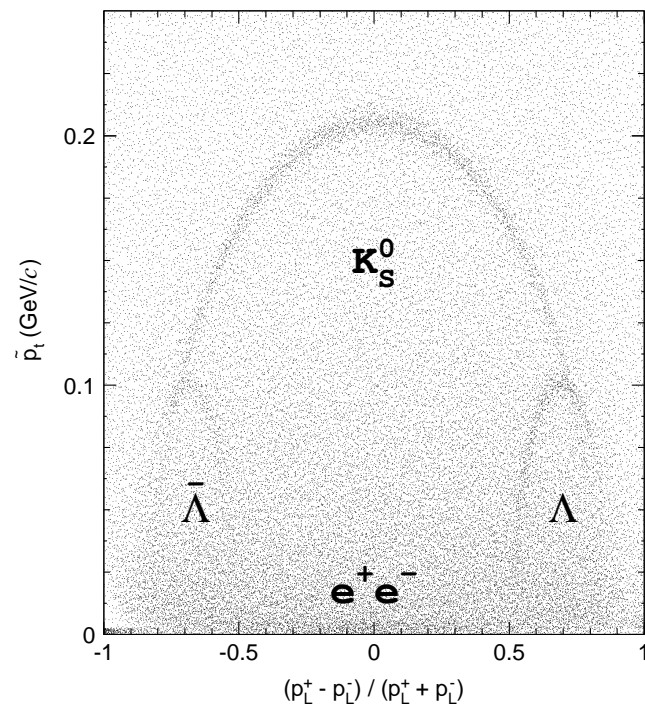


Figure 2: The Armenteros-Podolanski plot for the V^0 candidates: the transverse momentum \tilde{p}_t of the oppositely charged decay products vs. their asymmetry in longitudinal momenta p_L^\pm . All momenta are relative to the V^0 line-of-flight. Background from $\gamma \rightarrow e^+e^-$ conversions populates the region below $\tilde{p}_t = 0.015$ GeV/c.

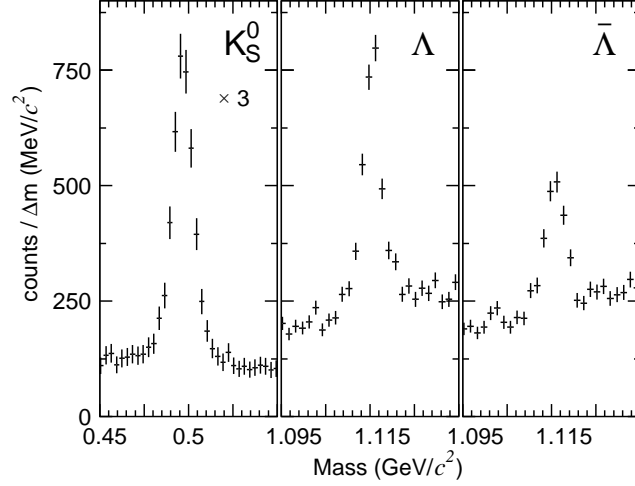


Figure 3: The invariant mass distributions for K_S^0 , Λ , and $\bar{\Lambda}$ particles summed over all runs with different targets. The size of the invariant mass bins (Δm) is $3.0 \text{ MeV}/c^2$ for the K_S^0 distribution and $1.5 \text{ MeV}/c^2$ otherwise.

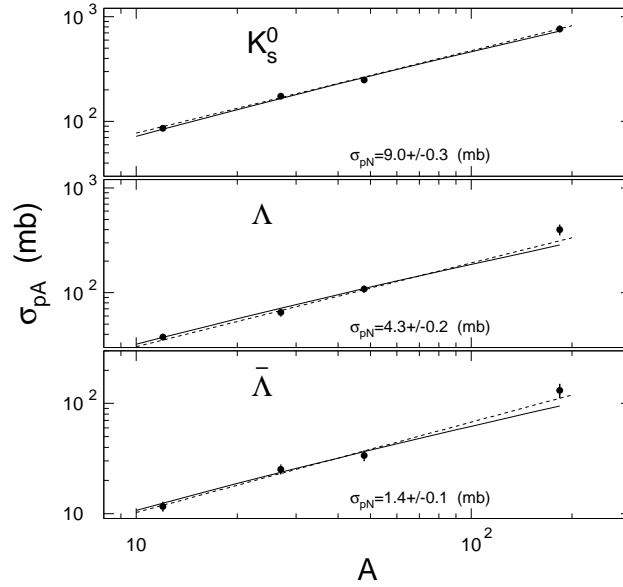


Figure 4: The V^0 total production cross sections σ_{pA} as a function of the atomic mass A of the target material. The solid lines show fits within the Glauber model, which yield the indicated production cross sections per nucleon (σ_{pN}). The dashed lines are fits to the form $\sigma_{pA} \propto A^\alpha$; the resultant α values are listed in Table 3.

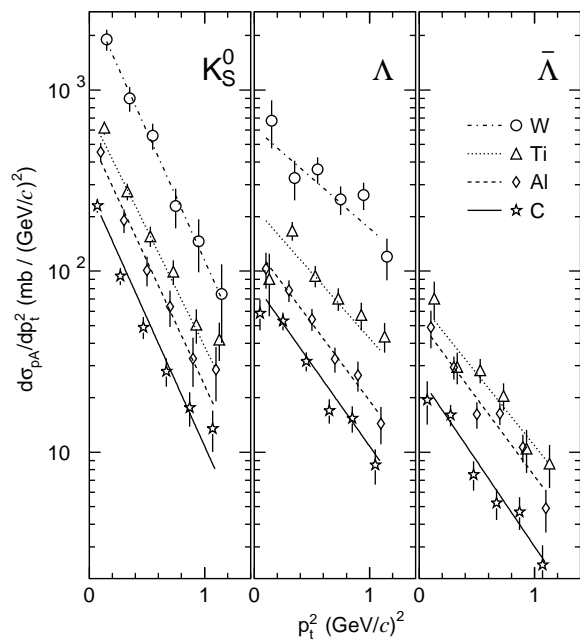


Figure 5: The differential cross section $d\sigma_{pA}/dp_t^2$ for K_S^0 , Λ , and $\bar{\Lambda}$ production on indicated target materials as obtained by extrapolation to the full x_F range $[-1, +1]$.

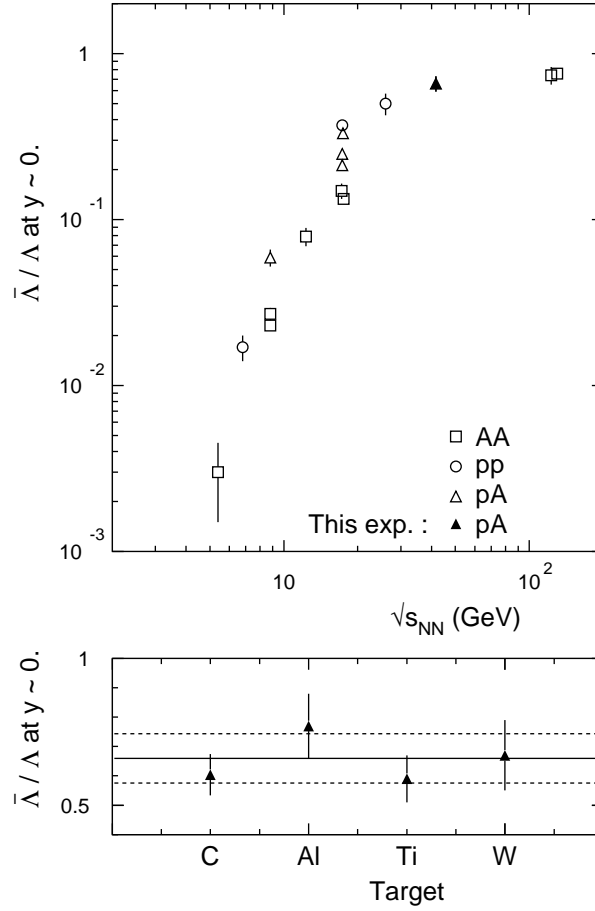


Figure 6: Top: The ratio of $\bar{\Lambda}$ and Λ particle yields at mid-rapidity for pp (circles), pA (triangles), and AA (squares) collisions as a function of the nucleon-nucleon center-of-mass energy $\sqrt{s_{NN}}$. The black triangle denotes the average of the HERA-B results; references for the open symbols are given in the text. Bottom: The ratio $d\sigma_{pA}(\bar{\Lambda})/d\sigma_{pA}(\Lambda)$ determined at $x_F \approx -0.06$ for the indicated targets; the average of the four values and the standard deviation are indicated by the solid and dashed lines, respectively.

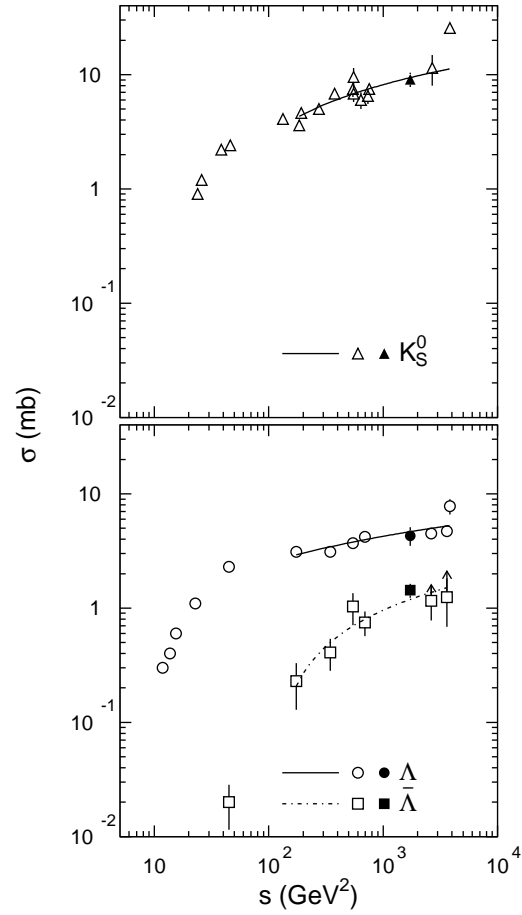


Figure 7: The total cross sections per nucleon σ_{pN} for the production of K_S^0 , Λ , and $\bar{\Lambda}$ particles as a function of s , the square of the center-of-mass energy. Black symbols denote the results from HERA-B, open symbols those from [6, 7, 8, 9, 10, 11, 12, 13, 14, 15, 16, 17, 18, 19, 20, 21, 22, 23, 24] and refs. therein. The curves are calculated using the fit functions reported in Ref. [18].